SCIENTIFIC REPORTS
nature research

Check for updates

OPEN

Investigation on the Electrochemical Performances of Mn_2O_3 as a Potential Anode for Na-Ion Batteries

Nor Fazila Mahamad Yusoff[1], Nurul Hayati Idris[1]✉, Muhamad Faiz Md. Din[2], Siti Rohana Majid[3], Noor Aniza Harun[4] & Md. Mokhlesur Rahman[5]✉

Currently, the development of the sodium-ion (Na-ion) batteries as an alternative to lithium-ion batteries has been accelerated to meet the energy demands of large-scale power applications. The difficulty of obtaining suitable electrode materials capable of storing large amount of Na-ion arises from the large radius of Na-ion that restricts its reversible capacity. Herein, Mn_2O_3 powders are synthesised through the thermal conversion of $MnCO_3$ and reported for the first time as an anode for Na-ion batteries. The phase, morphology and charge/discharge characteristics of Mn_2O_3 obtained are evaluated systematically. The cubic-like Mn_2O_3 with particle sizes approximately 1.0–1.5 µm coupled with the formation of Mn_2O_3 sub-units on its surface create a positive effect on the insertion/deinsertion of Na-ion. Mn_2O_3 delivers a first discharge capacity of 544 mAh g^{-1} and retains its capacity by 85% after 200 cycles at 100 mA g^{-1}, demonstrating the excellent cyclability of the Mn_2O_3 electrode. Therefore, this study provides a significant contribution towards exploring the potential of Mn_2O_3 as a promising anode in the development of Na-ion batteries.

Sodium-ion (Na-ion) batteries have been introduced as a possible alternative to lithium-based ion batteries due to several reasons, including abundant supply, low cost and less toxicity[1,2]. However, sodium cannot be simply swapped with lithium as sodium has a larger ion size (1.02 Å for Na^+ as compared to 0.76 Å for Li^+) and slightly different chemistry, resulting in sluggish reaction kinetics that usually causes low capacity, poor rate capability and poor cyclability[1,3–5]. Therefore, challenges still exist to find suitable anode materials for the development of Na-ion batteries and scientists are searching for the best material among a vast number of materials using the trial-and-error approach.

Among the various types of materials, metal oxides have been explored extensively for lithium-ion (Li-ion) batteries. Similar to Li-ion batteries, metal oxides can potentially be used as large capacity anodes for Na-ion batteries because of their high theoretical capacities resulting from conversion reaction in most cases. For example, one-step conversion reaction of metal oxide with Na-ions can deliver high theoretical specific capacities of >600 mAh g^{-1} according to the reaction described in Eq. (1)[6,7].

$$MO_x + 2x\mathrm{Na} + 2xe^- \leftrightarrow x\mathrm{Na_2O} + \mathrm{M(M = Co,\ Fe,\ Mn,\ Cu,\ etc.)} \quad (1)$$

Among different conversion-type transition metal oxides for anodes, manganese oxides exhibit advantages of high capacity, natural richness, low cost and environmental benignity. Even though manganese oxides including mono, Mn_3O_4, Mn_2O_3, MnO_2 and their carbon-based composites with different nanostructures have been found technologically important in Li-ion batteries[8], the use of manganese oxides in Na-ion batteries is rarely reported. In 2014, Jiang *et al.*[9] synthesised Mn_3O_4 and investigated its reactivity as anode towards sodium for the first time.

[1]Energy Storage Research Group, Faculty of Ocean Engineering Technology and Informatics, Universiti Malaysia Terengganu, 21030, Kuala Nerus, Terengganu, Malaysia. [2]Department of Electrical and Electronic Engineering, Faculty of Engineering, National Defence University of Malaysia, Kem Sungai Besi, 57000, Kuala Lumpur, Malaysia. [3]Center for Ionics University of Malaya, Department of Physics, Faculty of Science, University of Malaya, 50603, Kuala Lumpur, Malaysia. [4]Advance Nano Materials (ANOMA) Research Group, Faculty of Science and Marine Environment, Universiti Malaysia Terengganu, 21030, Kuala Nerus, Terengganu, Malaysia. [5]Institute for Frontier Materials, Deakin University, Waurn Ponds, Victoria, 3216, Australia. ✉e-mail: nurulhayati@umt.edu.my; m.rahman@deakin.edu.au

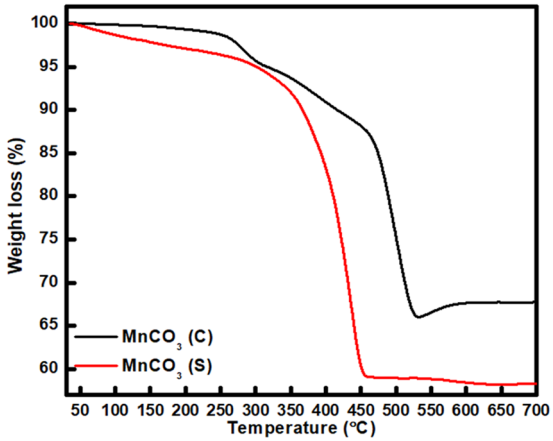

Figure 1. TGA curves of $MnCO_3$ (C) and $MnCO_3$ (S) at a heating rate of 10 °C min^{-1} in air.

Subsequently, Weng *et al.*[10] prepared MnO_2 using a SiO_2-templated hydrothermal approach, which was used as conversion-type anode for Na-ion batteries. However, rapid irreversible fading of capacities following the cycling process is a common problem with MnO_2 and Mn_3O_4 phases due to volume expansion and aggregation as well as low electronic conductivity. To tackle these problems with transition metal oxide anodes, nanostructure engineering is widely adopted, where structural parameters including particle size, crystal size and morphology act as critical factors in achieving maximum electrochemical performance. By adopting nanostructure engineering, much improvement of sodium storage properties was realised with MnO_2 anode by the development of new structures such as MnO_2 nanorods and nanoflowers[11,12].

In this study, Mn_2O_3 is synthesised by combining a hydrothermal and a thermal decomposition method and used as Na-ion battery anode for the first time. We developed a cubic structure of Mn_2O_3 by simple thermal decomposition of manganese carbonate ($MnCO_3$) precursor through controlled calcination temperatures. The crucial feature of this structure is that cubic particles of Mn_2O_3 are approximately 1–2 µm in size and are composed of numerous nanoparticles (sub-units) of 40–50 nm grown on the surface, leading to more accessible sites for electrolyte penetration into the bulk of the electrode, which facilitates ion transportation thereby promoting the insertion/deinsertion of Na-ions[13]. The obtained Mn_2O_3 anode prepared at 600 °C demonstrates an impressive capacity of 130 mAh g^{-1} at 100 mA g^{-1} after 200 cycles with a remarkable rate capability of 120 mAh g^{-1} at a very high current of 1000 mA g^{-1} even without any cation doping or carbon coating.

Results and Discussion

To verify the nature of decomposition and the formation temperature of Mn_2O_3, TGA analysis of both $MnCO_3$ precursors (synthesized $MnCO_3$ (denoted as $MnCO_3$ (S) and commercially available $MnCO_3$ ($MnCO_3$ (C)) was performed. It is clearly observed that the nature of decomposition of $MnCO_3$ (S) and $MnCO_3$ (C) precursors within the same temperature range is different, as shown in Fig. 1. One-step decomposition is realised with $MnCO_3$ (S), whereas $MnCO_3$ (C) precursor shows the two-step decomposition. Generally, the initial undulation appeared with initial weight loss of ~3 wt.% caused by the loss of hydrated water from $MnCO_3$. The weight loss appeared between 250 and 350 °C for $MnCO_3$ (C), presumably due to the formation of MnO_2 which is further confirmed by XRD analysis (Fig. S1). The commercial $MnCO_3$ (C) was heated up to temperature 300 °C in air for 2 h and the obtained product was analysed by XRD. The XRD pattern shows the presence of MnO_2 and $MnCO_3$ (C) in the product, suggesting partial decomposition of $MnCO_3$ (C) and formation of MnO_2[14]. It is obvious that the weight loss between 400 and 600 °C is attributed to the formation of Mn_2O_3 and the release of O_2[14–16]. Since only one-step decomposition slope is observed with $MnCO_3$ (S), the possible reaction during the decomposition of $MnCO_3$ (S) can be summarised as Eq. (2)[17,18]:

$$2MnCO_3 + O_2 \rightarrow Mn_2O_3 + 2CO_2 \quad (2)$$

Reducing the decomposition step of $MnCO_3$ (S) indicates that the conversion process is favourable since the kinetic process is shortened to obtain clear facet of Mn_2O_3.

Figure 2 shows the XRD patterns along with the Rietveld refinement profiles for $MnCO_3$ and Mn_2O_3. Figure 2(a) shows the refinement patterns for $MnCO_3$ (C) and $MnCO_3$ (S) precursors. All the diffraction peaks could be indexed to the rhodochrosite phase of $MnCO_3$ (JCPDS card No: 044-1472) with *R-3c* space group (rhombohedral unit cell). The refined lattice parameters for $MnCO_3$ (C) were $a = 4.8045$ (2) Å, $c = 15.6892$ (8) Å, and the unit cell volume was 313.636 $Å^3$ (Table S1). For $MnCO_3$ (S), the lattice parameters were smaller than $MnCO_3$ (C) with $a = 4.8019$ (3) Å, $c = 15.6798$ (1) Å and a unit cell volume of 313.103 $Å^3$ that are consistent with the previous report[19]. However, a small diffraction peak appeared at 2θ value of 28.5° for $MnCO_3$ (S), which is attributed to impurity that could have formed due to incomplete utilisation of manganese precursor during the hydrothermal process[20]. Furthermore, the average crystallite sizes (L) of $MnCO_3$ were calculated according to the Scherrer's equation as shown in Eq. (3):

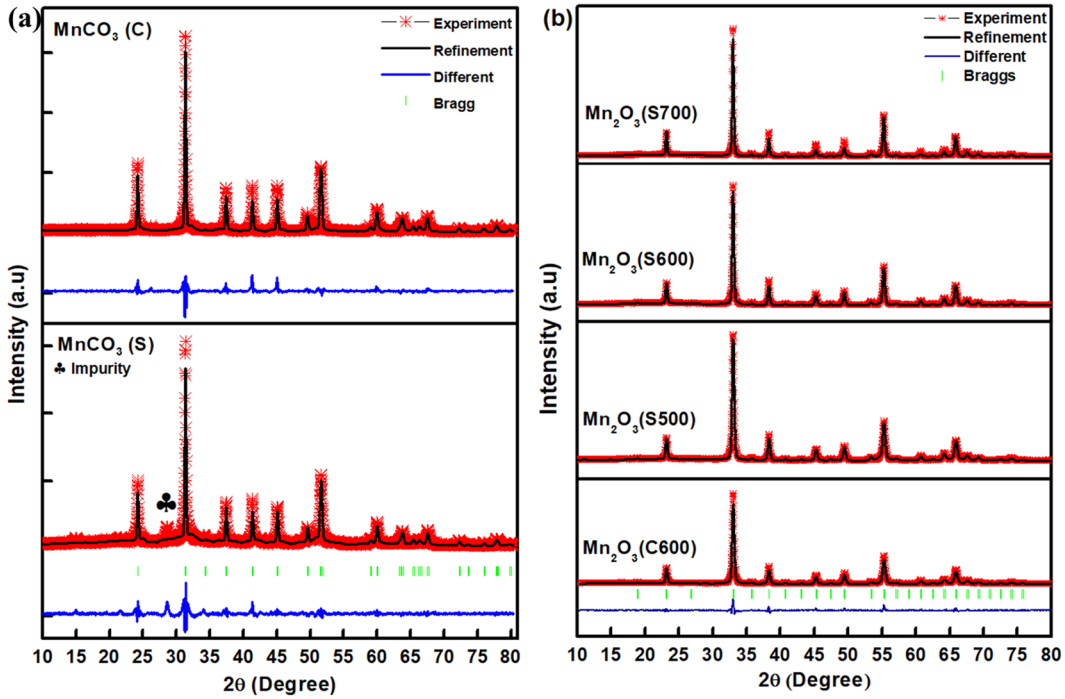

Figure 2. Rietveld refinement fits of the XRD data: (**a**) Commercial and synthesized $MnCO_3$; and (**b**) Mn_2O_3 (C600), Mn_2O_3 (S500), Mn_2O_3 (S600) and Mn_2O_3 (S700) powders.

$$L = \frac{k}{\beta \cos\theta} \tag{3}$$

where, k is the constant (0.9394), λ is the X-ray wavelength of Cu-Kα (1.5148 Å), β is the FWHM of the XRD peak in radian and θ is the angle of diffraction. The calculated average crystallite sizes of the $MnCO_3$ (C) and $MnCO_3$ (S) samples were ~36 nm and ~35 nm, respectively, which is in good agreement with reported result[21]. Figure 2(b) shows quantitative analysis of the Rietveld refinement fit profiles along with the observed XRD patterns of Mn_2O_3 (C600), Mn_2O_3 (S500), Mn_2O_3 (S600) and Mn_2O_3 (S700) samples. All the diffraction peaks matched well and could be indexed to a cubic Mn_2O_3 with the space group of *la-3* (JCPDS card no.041-1442). No other diffraction peaks of any impurities have been detected. As the calcination temperature increases, the intensity of the diffraction peaks of Mn_2O_3 increased, indicating improved crystallinity[22]. No changes were observed in the crystallite size of Mn_2O_3 (~23 nm) at the calcination temperature of 500 and 600 °C, whereas it was ~31 nm at 700 °C based on the (222) peak. Nevertheless, crystallite size decreases during transformation of $MnCO_3$ to Mn_2O_3. The details of lattice parameter, goodness of fit and other related fitting parameters of Mn_2O_3 obtained from crystal structure refinement are consistent with other reports[23,24]. Clearly, the lattice parameter of Mn_2O_3 increases as the calcination temperature increases due to the expansion during crystal growth.

Figure 3(a) shows FTIR spectra of D-glucose, $MnCO_3$ and Mn_2O_3 samples. The FTIR spectrum of D-glucose shows the existence of a strong and broad absorption peak at 3391 cm^{-1} indicating the presence of ν(OH) group stretching vibration. A small peak at 2920 cm^{-1} was attributed to the absorption peak of $\nu(CH_2)$ group, and the bands at 1475 cm^{-1} and 1328 cm^{-1} were assigned to the bending vibration of ν(CH). The ν(C–O) and ν(C–C) stretching bands were observed at 1132 and 1007 cm^{-1}, respectively[25,26]. During hydrothermal process, the D-glucose peaks (O–H bond at 3391 cm^{-1} and C–H bond at 1475 cm^{-1}) were completely vanished due to the formation of $MnCO_3$ (S) with the presence of C–O bending vibration of carbonate peaks at 1384, 860 and 721 cm^{-1} [27]. When $MnCO_3$ was heated at high temperature, the carbonate peaks diminished. The presence of three absorption peaks located at 487, 559 and 655 cm^{-1} for Mn_2O_3 may be attributed to Mn–O and Mn–O–Mn, confirming the formation of Mn_2O_3[25,27,28], which is consistent with the Raman spectroscopy results as shown in Fig. 3(b). Raman active bands located at 170–1000 cm^{-1} may be due to the Mn–O vibration modes of manganese oxides[29,30]. The Raman bands at 310, 366 and 655 cm^{-1} are corresponding to the bending modes of Mn_2O_3, the asymmetric stretch of Mn–O–Mn and an asymmetric stretch of Mn_2O_3 corresponding to Mn (III)–O mode vibration group, respectively[25].

Surface morphologies of $MnCO_3$ (C) and $MnCO_3$ (S) precursors were examined using SEM analysis, as depicted in Fig. S2. SEM analysis reveals that particles are agglomerated clusters and non-uniformly distributed with a size of 0.5–1.5 µm. It is clearly observed that Mn_2O_3 (C600) obtained from $MnCO_3$ (C) precursor possesses irregular shape with an approximate particle size between 0.5 and 1.3 µm (Fig. 4(a)). Conversely, well-defined cubic particles of Mn_2O_3 were formed through the calcination of $MnCO_3$ (S) precursor (Fig. 4(b–d)). Mn_2O_3 (S500) consists of inhomogeneous cubic particles in the range of 1.0−1.2 µm in sizes (Fig. 4(b)). Mn_2O_3 (S600)

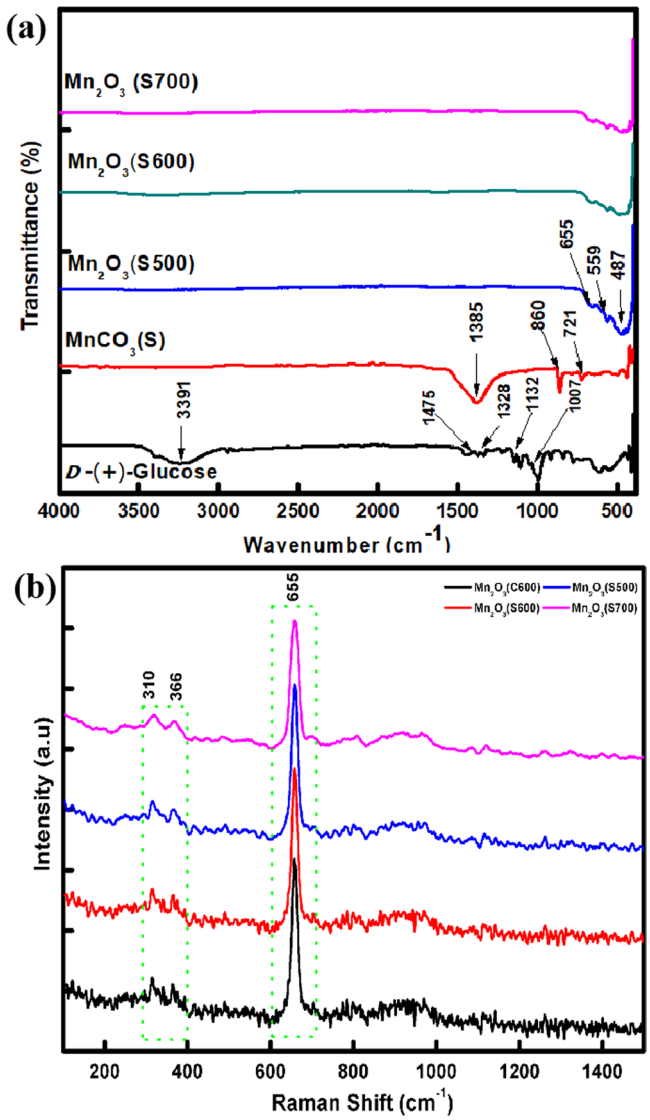

Figure 3. (**a**) FTIR spectra of D-glucose, $MnCO_3$ (S), Mn_2O_3 (S500), Mn_2O_3 (S600) and Mn_2O_3 (S700); and (**b**) Raman spectra of Mn_2O_3 (C600), Mn_2O_3 (S500), Mn_2O_3 (S600) and Mn_2O_3 (S700).

exhibits larger cubic particles (0.9−1.7 µm sizes) (Fig. 4(c)) with numerous nanoparticles (sub-units) observed on the surface. Moreover, cubic Mn_2O_3 are organised by nanosized sub-units (40−50 nm) with distinct voids between the sub-units (Fig. S3). The *d*-spacing of 0.38 nm of the sample corresponded well with (211) lattice plane of Mn_2O_3 (Fig. S4). Clearly, well-defined cubic particles of Mn_2O_3 were observed with an average size of approximately 1.1−1.7 µm, when the precursor was calcined at a high temperature of 700 °C (Fig. 4(d)). Moreover, a porous-like structure is clearly visible at the surface of the cubic at 700 °C. This type of structure is often formed if metal carbonate is used as a precursor because it releases O_2 and CO_2 from the interior of the metal carbonate, which possibly leads to a finer or porous structure[13,14,16]. The obtained electron microscopy results demonstrate that one-step decomposition of the synthesised $MnCO_3$ precursor produces a clear facet with well-defined cubic Mn_2O_3 structures compared to the two-step decomposition of the commercial $MnCO_3$. The hysteresis loops (Fig. S5) reveal that these materials exhibit type IV isotherm, indicating a disordered mesoporous structure with average pore diameter between 5 and 60 nm. The calculated BET specific surface area for the Mn_2O_3 powders are tabulated in Table S2. It is well known that nanostructures play a crucial role in electrochemical processes due to their capability to enhance mass diffusion and transportation such as electrolyte penetration or ion transport[31]. Moreover, porous-like nanostructures can allow an electrolyte to diffuse smoothly within the lattice fringes of the crystals, providing more active sites and shortened ion route. Such structures are also beneficial because they relieve the stress and buffer the volume changes caused by pulverisation and aggregation process during redox reaction[32,33]. Therefore, the structure of Mn_2O_3 obtained from $MnCO_3$ (S) precursor is likely to enhance Na-ion storage performance.

The galvanostatic charge/discharge measurements of the Mn_2O_3 electrodes at a current density of 100 mA g^{-1} within the potential range of 0.01−3.00 V (vs. Na/Na^+) are shown in Fig. 5. At the first cycle, irreversible capacities

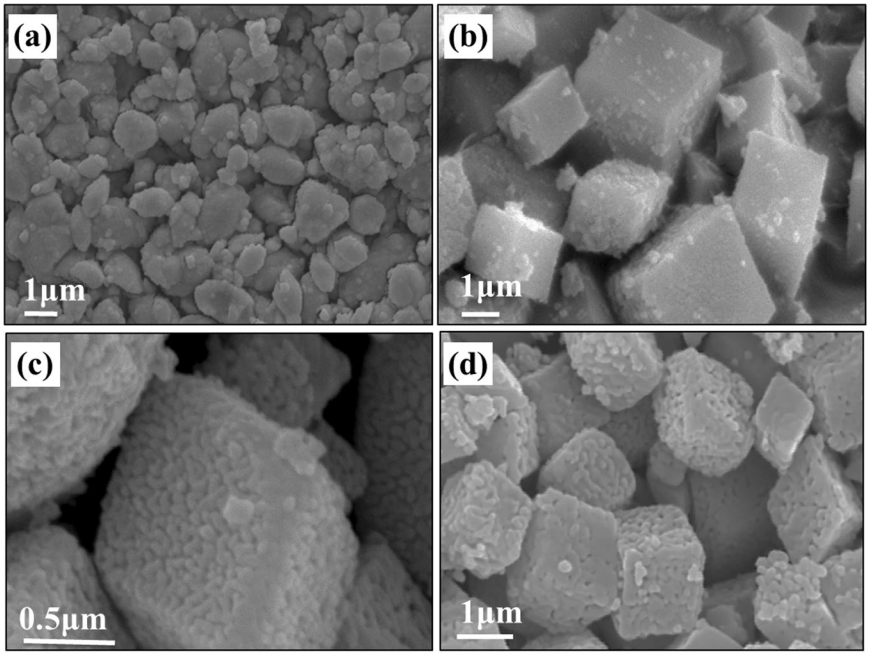

Figure 4. SEM images of (**a**) Mn_2O_3 (C600), (**b**) Mn_2O_3 (S500), (**c**) Mn_2O_3 (S600) and (**d**) Mn_2O_3 (S700).

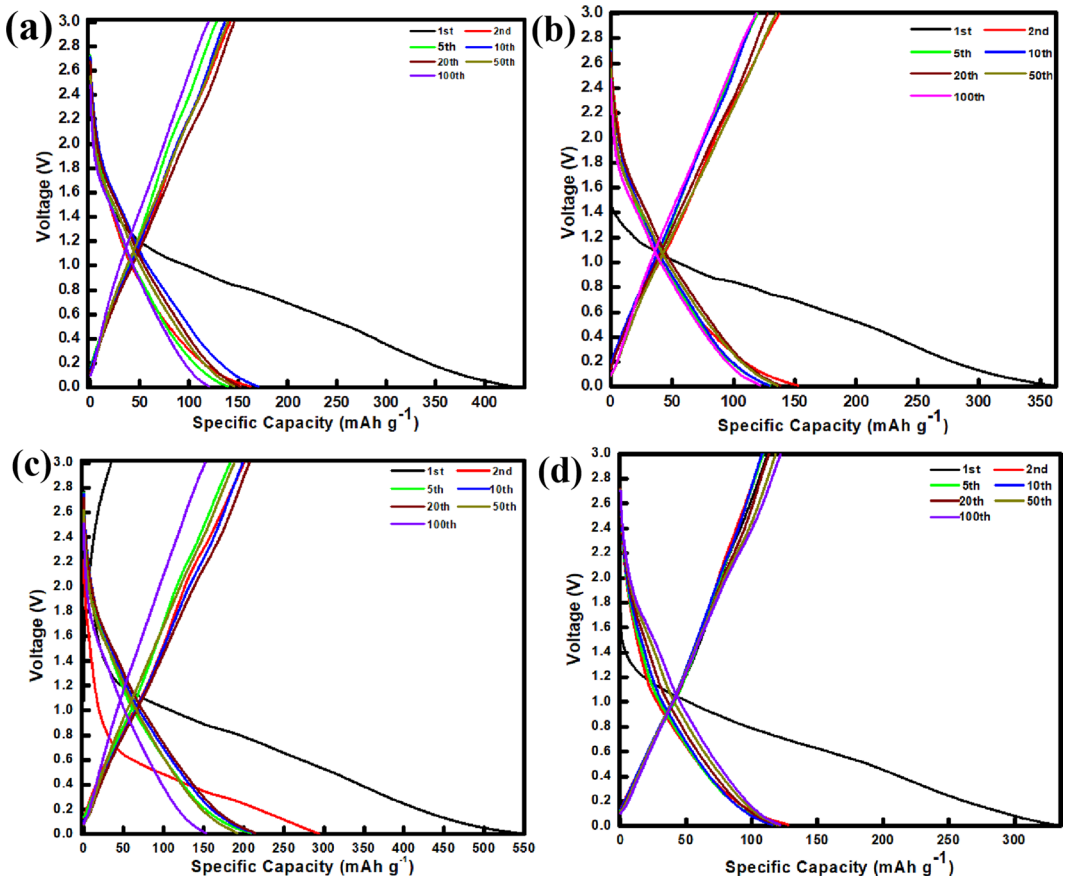

Figure 5. Galvanostatic charge/discharge profiles of (**a**) Mn_2O_3 (C600), (**b**) Mn_2O_3 (S500), (**c**) Mn_2O_3 (S600), and (**d**) Mn_2O_3 (S700).

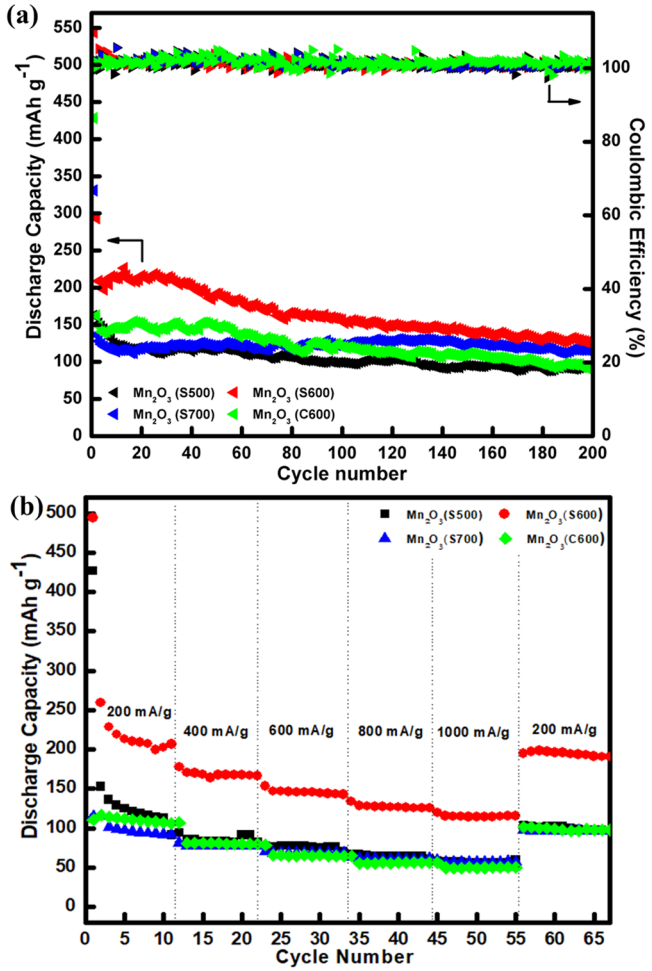

Figure 6. (**a**) Cycling performances and the Coulombic efficiencies up to 200 cycles at 100 mA g^{-1} and (**b**) rate capability for the Mn_2O_3 electrodes.

observed in all electrodes may be attributed to the undesirable growth of a surface passivation layer of solid electrolyte interphase (SEI). The discharge/charge potential profile of the Mn_2O_3 (S600) electrode was further supported by CV analysis as demonstrated in Fig. S6. However, the SEI formation plateau for the Na/Na^+ system is not as sharp/long as compared to the Li-ion cell[34,35]. Conversely, no distinct plateau observed in the charge/discharge curves after the first cycle, typically seen and consistent with other metal oxides anode in the Na/Na^+ system[10,12,36–38]. During cathodic process, Mn and Na_2O were observed from the *ex-situ* XRD patterns (Fig. S7), whereas, re-formation of Mn_2O_3 was observed during anodic process. It is important to note that the evidence of Mn phase formation is hardly found in the XRD patterns because of significant overlap of this Mn peak with very strong peak from copper (Cu) current collector. Therefore, the formation of Mn and Na_2O and the re-formation of Mn_2O_3 can be expressed by the following electrochemical reversible conversion reaction in Eq. (4).

$$Mn_2O_3 + 6Na^+ + 6e^- \leftrightarrow 2Mn + 3Na_2O \quad (4)$$

Figure 6 shows the cycling performance of the Mn_2O_3 electrodes. Figure 6(a) compares cycling stability and Coulombic efficiency among the electrodes measured at a current density of 100 mA g^{-1} up to 200 cycles. All electrodes exhibit high initial discharge capacity of 544 mAh g^{-1} for Mn_2O_3 (S600), 429 mAh g^{-1} for Mn_2O_3 (C600), 331 mAh g^{-1} for Mn_2O_3 (S700) and 163 mAh g^{-1} for Mn_2O_3 (S500). High initial discharge capacity could be related to the formation of SEI layer and the electrolyte decomposition itself[39]. For Mn_2O_3 (S600) electrode, the discharge capacity increased after the 2nd cycle and then started to decrease after ~15 cycles. Similar trends were observed for Mn_2O_3 (S700) electrode, where the discharge capacity increased gradually and then started to decrease after 140 cycles, which was possibly due to the activation and stabilisation processes within the electrode[40–44]. Nevertheless, the capacity depletion behaviour was noticed in Mn_2O_3 (S500) and Mn_2O_3 (C600) electrodes. At 2nd cycle, the Mn_2O_3 (S600) electrode exhibited the highest discharge capacity of 294 mAh g^{-1} and gradually decreased to 130 mAh g^{-1} after 200 cycles. For the Mn_2O_3 (S700) electrode, the discharge capacity was 137 mAh g^{-1} at 2nd cycle and reached 116 mAh g^{-1} after 200 cycles. In the case of Mn_2O_3 (S500) and Mn_2O_3 (C600) electrodes, the discharge capacity at the 2nd cycle was 243 and 162 mAh g^{-1}, respectively. After 200 cycles,

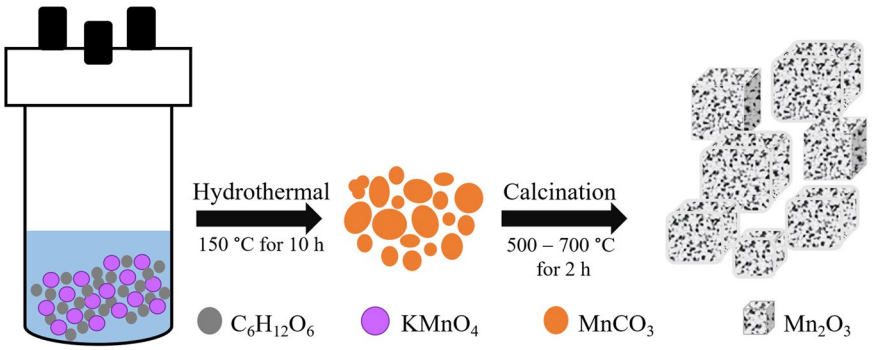

Scheme 1. A schematic presentation for the formation of Mn_2O_3.

both electrodes had the lowest discharge capacity, i.e. 66 mAh g^{-1} and 89 mAh g^{-1}. After the initial cycle, all electrodes showed very high Coulombic efficiency of approximately 100% throughout the cycles.

Rate capability of the Mn_2O_3 electrodes were also measured at different charge/discharge current densities and sustained for 11 cycles for each current density (Fig. 6(b)). At the initial 11th cycle, the Mn_2O_3 (S600) electrode delivered a high discharge capacity of 207 mAh g^{-1} at 200 mA g^{-1}. When the current density increased, the electrode exhibited high retention of 166 mAh g^{-1} at 400 mA g^{-1}, 143 mAh g^{-1} at 600 mA g^{-1}, 126 mAh g^{-1} at 800 mA g^{-1} and 115 mAh g^{-1} at 1000 mA g^{-1}. Moreover, consecutive cycling performances of Mn_2O_3 (S500), Mn_2O_3 (S700) and Mn_2O_3 (C600) electrodes were not as good as Mn_2O_3 (S600). Returning to 200 mA g^{-1} after it had been exposed to different discharge rates, the Mn_2O_3 (S600) electrode was able to restore the discharge capacity of 197 mAh g^{-1}, which represents above 90% capacity recovery.

All the above results show that cubic-like Mn_2O_3 demonstrates a possible insertion/deinsertion of Na-ion with a reasonable capacity and cycling stability. The key factor that contributes to the improved performances may be offered by the special morphology of Mn_2O_3 itself. It is well known that the surface area is proportional to the insertion sites for ions movements[45] and this could be ameliorated by downsizing the materials or porous architectures. The Mn_2O_3 synthesised here is cubic-like particles with nanoparticles (sub-units) embedded on their surfaces which in turn improve the electrochemical performances of the battery. Such Mn_2O_3 structure can be obtained by thermal decomposition of high quality starting metal source. Thermal decomposition of commercial $MnCO_3$ produced irregular shapes of Mn_2O_3 whereas, hydrothermally synthesised $MnCO_3$ resulted in cubic-like Mn_2O_3 particles. It is important to highlight that the use of glucose as reducing agent gives advantages to the precursor for growth in a required direction, thus developing well-crystallised $MnCO_3$ particles via the simple route with good reproducibility. Without using any scarifying template to form porous-like structure, this method is practical for scaling-up production in the industry. Clearly, the electrochemical characteristics of Mn_2O_3 in Na-ion storage is promising and needs to be further explored. The cubic-like Mn_2O_3 with nanoparticles on its surface provides more accessible sites for electrolyte penetration into inner Mn_2O_3 and exposes a large area for Na-ions transportation. Meanwhile, a short ion diffusion path could facilitate the charge-transfer and greatly improve the rate capability of the Na-ions. Additionally, porous-like structure of Mn_2O_3 could suppress the stress created by volume changes during insertion/deinsertion process. Overall, the electrochemical activity, i.e. synthesis process, discharge capacity and rate capability, demonstrated by Mn_2O_3 in this study is quite impressive. The performance of Mn_2O_3 anode can be further improved by controlled synthesis of highly porous nanostructured with high surface area. Such a porous nanostructured needs to be integrated with conductive matrix such as surface carbon coating or hybrid formation with graphite or graphene or carbon nanotubes[46–48]. These carbon materials will not only enhance electrical conductivities of the Mn_2O_3 electrodes, but also will prevent agglomeration of nanostructured Mn_2O_3 active materials during repeated cycling, leading to much improved electrochemical performance in terms of capacity, stability, and rate capability. The findings obtained from this research create opportunities for other researchers to explore this material as an anode for Na-ion batteries.

Materials and Methods

Synthesis of $MnCO_3$ and Mn_2O_3. Scheme 1 shows the synthesis strategy of Mn_2O_3 from the starting materials. To prepare $MnCO_3$, 0.3 mmol *D*-(+)-glucose ($C_6H_{12}O_6$, Merck Millipore) and 0.3 mmol $KMnO_4$ (Sigma-Aldrich, 97%) were dissolved in 60 ml deionised water at room temperature and stirred to form a homogeneous solution. Then, the homogeneous mixture was transferred into a 125 ml stainless steel autoclave, sealed and heated at 150 °C for 10 h. During the hydrothermal reaction, MnO_4^- was reduced by glucose and Mn^{2+} ions generated, leading to the formation of $MnCO_3$ according to the Eq. (5) below[49,50].

$$24KMnO_4 + 5C_6H_{12}O_6 = 24MnCO_3 + 6K_2CO_3 + 12KOH + 24H_2O \quad (5)$$

The precipitates were collected, washed several times with absolute ethanol and deionised water and dried overnight under vacuum. The dried sample is marked as ($MnCO_3$ (S)). To obtain Mn_2O_3, $MnCO_3$ (S) was calcined at 500, 600 and 700 °C in air for 2 h and denoted as Mn_2O_3 (S500), Mn_2O_3 (S600) and Mn_2O_3 (S700), respectively. For comparison purpose, as-received $MnCO_3$ (Sigma-Aldrich, 98%) marked as $MnCO_3$ (C) was also used in this study. $MnCO_3$ (C) was calcined at 600 °C in air for 2 h and later denoted as Mn_2O_3 (C600).

Materials characterization. The phase purity and structure of $MnCO_3$ and Mn_2O_3 samples were determined by X-ray diffraction (XRD, Rigaku Miniflex II) with monochromatic CuKα radiation at a wavelength (λ) of 1.5406 Å. The morphology of the samples was observed through scanning electron microscopy (SEM, JOEL JSM-6360L) and transmission electron microscopy (TEM, TECNAI G2 F20) with an accelerating voltage of 200 kV. The thermogravimetric analysis (TGA) was conducted on Mettler-Toledo thermogravimetric analysis/differential scanning calorimetry (TGA/DSC 1) Star^e System at a heating rate of 10 °C min^{-1} in air. The Fourier transform infra-red (FTIR) spectroscopy was recorded on an IR Tracer-100. Raman spectra were collected on Raman spectroscopy (Renishaw, 532 nm radiation) extended with 0.1 power laser measurement.

Electrochemical measurements. To investigate the electrochemical performances of Mn_2O_3 samples, the active materials, carbon black (Sigma-Aldrich, >99.95%) and poly(vinylidene fluoride) (PVDF, Sigma-Aldrich), in a weight ratio of 75:20:5 were dissolved in an *N*-methylpyrrolidone (NMP). The slurry was pasted onto a copper (Cu) foil with an approximate active material loading of ~ 2 mg cm^{-2}. The electrodes were then dried at 100 °C overnight under vacuum. Subsequently, the electrode was cut to 1 cm × 1 cm size. Coin-type cell (CR 2032) was assembled in an Argon-filled glove box (Mbraun, Unilab, Germany) using sodium metal (Sigma-Aldrich, 99.9% trace metals basis) as the counter electrode. A Whatman glass fibre (GF/D) was used as a separator, and the electrolyte 1 M $NaClO_4$ (Sigma-Aldrich, 98%), was dissolved in propylene carbonate (PC) (Sigma-Aldrich, anhydrous, 99.7%) with the addition of 5 wt.% of fluoroethylene carbonate (FEC) (Sigma-Aldrich, 99%). The cycling performance of the electrodes was conducted by Neware battery tester at room temperature.

Conclusion

The cubic-like Mn_2O_3 was successfully obtained through thermal decomposition of the hydrothermally synthesised $MnCO_3$. For comparison, Mn_2O_3 obtained through thermal conversion of commercial $MnCO_3$ was also investigated. The synthesis method employed in this study offers a simple and practical approach to industrial production. A microstructure of cubic-like Mn_2O_3 with nanoparticles (sub-units) embedded on its surface was obtained. The electrochemical results indicate that the Mn_2O_3 electrode can deliver a promising discharge capacity, cyclability and rate capability during the insertion/deinsertion of Na-ions. The Mn_2O_3 electrode exhibited high initial discharge capacity of 544 mAh g^{-1} at 100 mA g^{-1} and reached 130 mAh g^{-1} after 200 cycles. The obtained Mn_2O_3 structure promotes electrolyte penetration into the interior of Mn_2O_3, provides large sites to facilitate fast ion transportation and thus, expedites the charge-transfer within the electrode. Therefore, the results demonstrate strong evidence for its application in Na-ion batteries.

Received: 28 March 2020; Accepted: 15 May 2020;
Published online: 08 June 2020

References

1. Li, L. *et al*. Recent progress on sodium ion batteries: Potential high-performance anodes. *Energy Environ. Sci.* **11**, 2310–2340 (2018).
2. Vaalma, C., Buchholz, D., Weil, M. & Passerini, S. A cost and resource analysis of sodium-ion batteries. *Nat. Rev. Mater* **3**, 18013 (2018).
3. Ni, J., Bi, X., Jiang, Y., Li, L. & Lu, J. Bismuth chalcogenide compounds Bi2 × 3 (X = O, S, Se): Applications in electrochemical energy storage. *Nano Energy* **34**, 356–366 (2017).
4. Ni, J. & Li, L. Self-supported 3D array electrodes for sodium microbatteries. *Adv. Funct. Mater.* **28**, 1704880 (2018).
5. Adelhelm, P. *et al*. From lithium to sodium: cell chemistry of room temperature sodium–air and sodium–sulfur batteries. *Beilstein J. Nanotechnol.* **6**, 1016–1055 (2015).
6. Kim, Y., Ha, K. H., Oh, S. M. & Lee, K. T. High-capacity anode materials for sodium-ion batteries. *Chem. Eur. J* **20**, 11980–11992 (2014).
7. Kang, H. *et al*. Update on anode materials for Na-ion batteries. *J. Mater. Chem. A* **3**, 17899–17913 (2015).
8. Reddy, M., Subba Rao, G. & Chowdari, B. Metal oxides and oxysalts as anode materials for Li ion batteries. *Chem. Rev.* **113**, 5364–5457 (2013).
9. Jiang, Y. *et al*. Transition metal oxides for high performance sodium ion battery anodes. *Nano Energy* **5**, 60–66 (2014).
10. Weng, Y.-T. *et al*. An unexpected large capacity of ultrafine manganese oxide as a sodium-ion battery anode. *Nanoscale* **7**, 20075–20081 (2015).
11. Kim, S. W., Seo, D. H., Ma, X., Ceder, G. & Kang, K. Electrode materials for rechargeable sodium-ion batteries: Potential alternatives to current lithium-ion batteries. *Adv. Energy Mater.* **2**, 710–721 (2012).
12. Zhang, Z., Zhao, X. & Li, J. Facile synthesis of nanostructured MnO2 as anode materials for sodium-ion batteries. *ChemNanoMat* **2**, 196–200 (2016).
13. Huang, S.-Z. *et al*. Three-dimensional (3D) bicontinuous hierarchically porous Mn_2O_3 single crystals for high performance lithium-ion batteries. *Sci. Rep.* **5**, 14686 (2015).
14. Wang, L. *et al*. A general single-source route for the preparation of hollow nanoporous metal oxide structures. *Angew. Chem. Int. Ed* **48**, 7048–7051 (2009).
15. Liu, L., Yang, Z., Liang, H., Yang, H. & Yang, Y. Facile synthesis of MnCO3 hollow dumbbells and their conversion to manganese oxide. *Mater. Lett.* **64**, 2060–2063 (2010).
16. Pudukudy, M., Yaakob, Z. & Rajendran, R. Facile synthesis of mesoporous α-Mn_2O_3 microspheres via morphology conserved thermal decomposition of MnCO3 microspheres. *Mater. Lett.* **136**, 85–89 (2014).
17. Yang, L.-X., Zhu, Y.-J., Tong, H. & Wang, W.-W. Submicrocubes and highly oriented assemblies of $MnCO_3$ synthesized by ultrasound agitation method and their thermal transformation to nanoporous Mn_2O_3. *Ultrason. Sonochem.* **14**, 259–265 (2007).
18. Fang, Y. *et al*. Synthesis of unique hierarchical mesoporous layered-cube Mn_2O_3 by dual-solvent for high-capacity anode material of lithium-ion batteries. *Chem. Eng. J.* **315**, 583–590 (2017).
19. Devaraj, S., Liu, H. & Balaya, P. $MnCO_3$: a novel electrode material for supercapacitors. *J. Mater. Chem. A* **2**, 4276–4281 (2014).
20. Vardhan, P. V., Jothilakshmi, C., Mudali, U. K. & Devaraj, S. The effect of carbonate precursors on the capacitance properties of $MnCO_3$. *Mater. Today: Proc* **4**, 12407–12415 (2017).
21. Karuppaiah, M. *et al*. Formation of one dimensional nanorods with microsphere of $MnCO_3$ using Ag as dopant to enhance the performance of pseudocapacitors. *Mater. Chem. Phys.* **228**, 1–8 (2019).
22. Lou, X. W., Deng, D., Lee, J. Y. & Archer, L. A. Thermal formation of mesoporous single-crystal Co_3O_4 nano-needles and their lithium storage properties. *J. Mater. Chem.* **18**, 4397–4401 (2008).

23. Chandra, M. *et al*. Multiferroicity and magnetoelastic coupling in $\alpha-Mn_2O_3$: A binary perovskite. *Phys. Rev. B* **98**, 104427 (2018).
24. Geller, S. Structure of α-Mn_2O_3, $(Mn0.983Fe0.017)2O_3$ and $(Mn0.37Fe0.63)2O_3$ and relation to magnetic ordering. *Acta Crystallogr. Sect. B* **27**, 821–828 (1971).
25. Liang, J., Bu, L.-T., Cao, W.-G., Chen, T. & Cao, Y.-C. Facile fabrication of coaxial-cable like Mn_2O_3 nanofiber by electrospinning: Application as electrode material for supercapacitor. *J. Taiwan Inst. Chem. Eng.* **65**, 584–590 (2016).
26. Ibrahim, M., Alaam, M., El-Haes, H., Jalbout, A. F. & Leon, A. D. Analysis of the structure and vibrational spectra of glucose and fructose. *Ecletica Quim* **31**, 15–21 (2006).
27. Sekhar, B. C., Babu, G. & Kalaiselvi, N. Nanoflake driven Mn_2O_3 microcubes modified with cooked rice derived carbon for improved electrochemical behavior. *RSC Adv.* **5**, 4568–4577 (2015).
28. Chen, H. & He, J. Facile synthesis of monodisperse manganese oxide nanostructures and their application in water treatment. *J. Phys. Chem. C* **112**, 17540–17545 (2008).
29. Javed, Q. *et al*. Diameter-controlled synthesis of α-Mn_2O_3 nanorods and nanowires with enhanced surface morphology and optical properties. *Nanotechnol* **23**, 415603 (2012).
30. Han, Y.-F. *et al*. Observation of the reversible phase-transformation of α-Mn_2O_3 nanocrystals during the catalytic combustion of methane by *in situ* Raman spectroscopy. *J. Phys. Chem. C* **111**, 2830–2833 (2007).
31. Li, W. *et al*. Facile synthesis of porous Mn_2O_3 nanocubics for high-rate supercapacitors. *Electrochim. Acta* **157**, 108–114 (2015).
32. Zeng, K. *et al*. Cave-embedded porous Mn_2O_3 hollow microsphere as anode material for lithium ion batteries. *Electrochim. Acta* **247**, 795–802 (2017).
33. Wu, F., Bai, J., Feng, J. & Xiong, S. Porous mixed metal oxides: Design, formation mechanism, and application in lithium-ion batteries. *Nanoscale* **7**, 17211–17230 (2015).
34. Guo, X. *et al*. Surfactant-free scalable synthesis of hierarchically spherical Co_3O_4 superstructures and their enhanced lithium-ion storage performances. *Nanotechnol* **23**, 465401 (2012).
35. Yang, X. *et al*. Tailored graphene-encapsulated mesoporous Co_3O_4 composite microspheres for high-performance lithium ion batteries. *J. Mater. Chem.* **22**, 17278–17283 (2012).
36. Wang, L. *et al*. Metal oxide/graphene composite anode materials for sodium-ion batteries. *Energy Storage Mater* **16**, 434–454 (2019).
37. Kumar, P. R., Jung, Y. H., Bharathi, K. K., Lim, C. H. & Kim, D. K. High capacity and low cost spinel Fe_3O_4 for the Na-ion battery negative electrode materials. *Electrochim. Acta* **146**, 503–510 (2014).
38. Tang, J. *et al*. The electrochemical performance of NiO nanowalls/Ni anode in half-cell and full-cell sodium ion batteries. *Mater. Lett.* **195**, 127–130 (2017).
39. Gao, L., Gu, C., Zhao, J., Song, X. & Huang, J. Preparation of manganese monoxide@ reduced graphene oxide nanocomposites with superior electrochemical performances for lithium-ion batteries. *Ceram. Int* **45**, 3425–3434 (2019).
40. Shaju, K. M., Jiao, F., Débart, A. & Bruce, P. G. Mesoporous and nanowire Co_3O_4 as negative electrodes for rechargeable lithium batteries. *Phys. Chem. Chem. Phys.* **9**, 1837–1842 (2007).
41. Marzuki, N. S., Taib, N. U., Hassan, M. F. & Idris, N. H. Enhanced lithium storage in Co_3O_4/carbon anode for Li-ion batteries. *Electrochim. Acta* **182**, 452–457 (2015).
42. Rosedhi, N. D., Idris, N. H., Rahman, M. M., Din, M. M. & Wang, J. Disordered spinel $LiNi0.5Mn1.5O_4$ cathode with improved rate performance for lithium-ion batteries. *Electrochim. Acta* **206**, 374–380 (2016).
43. Idris, N. H., Rahman, M. M., Wang, J.-Z., Chen, Z.-X. & Liu, H.-K. Synthesis and electrochemical performance of LiV_3O_8/carbon nanosheet composite as cathode material for lithium-ion batteries. *Compos. Sci. Technol.* **71**, 343–349 (2011).
44. Sakunthala, A. *et al*. Synthesis and electrochemical studies on LiV_3O_8. *J. Solid State Electrochem* **14**, 1847–1854 (2010).
45. Allen, J., Jow, T. & Wolfenstine, J. Low temperature performance of nanophase $Li_4Ti_5O_{12}$. *J. Power Sources* **159**, 1340–1345 (2006).
46. Dai, L., Chang, D. W., Baek, J. B. & Lu, W. Carbon nanomaterials for advanced energy conversion and storage. *Small* **8**, 1130–1166 (2012).
47. Ni, J. *et al*. A review on integrating nano-carbons into polyanion phosphates and silicates for rechargeable lithium batteries. *Carbon* **92**, 15–25 (2015).
48. Ni, J. & Li, Y. Carbon nanomaterials in different dimensions for electrochemical energy storage. *Adv. Energy Mater.* **6**, 1600278 (2016).
49. Rubinsztain, Y., Yariv, S., Ioselis, P., Aizenshtat, Z. & Ikan, R. Characterization of melanoidins by IR spectroscopy—II. Melanoidins of galactose with arginine, isoleucine, lysine and valine. *Org. Geochem.* **9**, 371–374 (1986).
50. Wang, R. *et al*. A cost effective, highly porous, manganese oxide/carbon supercapacitor material with high rate capability. *J. Mater. Chem. A* **4**, 5390–5394 (2016).

Acknowledgements

The authors acknowledge Universiti Malaysia Terengganu for providing the financial support under Talent And Publication Enhancement-Research Grant (TAPE-RG; vot no. 55158).

Author contributions

N.H.I. and N.F.M.Y. conceived the idea and designed the experiments, and wrote the manuscript. N.F.M.Y. carried out most of the experimental work. M.F.M.D., S.R.M., N.A.H. and M.M.R. assists the experimental work and data analysis. All authors involved in the discussion to finalize the manuscript.

Competing interests

The authors declare no competing interests.

Additional information

Supplementary information is available for this paper at https://doi.org/10.1038/s41598-020-66148-w.

Correspondence and requests for materials should be addressed to N.H.I. or M.M.R.

Reprints and permissions information is available at www.nature.com/reprints.

Publisher's note Springer Nature remains neutral with regard to jurisdictional claims in published maps and institutional affiliations.

Open Access This article is licensed under a Creative Commons Attribution 4.0 International License, which permits use, sharing, adaptation, distribution and reproduction in any medium or format, as long as you give appropriate credit to the original author(s) and the source, provide a link to the Creative Commons license, and indicate if changes were made. The images or other third party material in this article are included in the article's Creative Commons license, unless indicated otherwise in a credit line to the material. If material is not included in the article's Creative Commons license and your intended use is not permitted by statutory regulation or exceeds the permitted use, you will need to obtain permission directly from the copyright holder. To view a copy of this license, visit http://creativecommons.org/licenses/by/4.0/.

© The Author(s) 2020